Dalton Transactions

RSC Publishing

PAPER

View Article Online
View Journal | View Issue

Cite this: *Dalton Trans.*, 2013, **42**, 12675

Precision synthesis of silicon nanowires with crystalline core and amorphous shell

Timothy D. Bogart, Xiaotang Lu and Brian A. Korgel*

Received 2nd April 2013,
Accepted 30th April 2013

DOI: 10.1039/c3dt50875g

www.rsc.org/dalton

A synthetic route to crystalline silicon (Si) nanowires with an amorphous Si shell is reported. Trisilane (Si_3H_8) and $Sn(HMDS)_2$ are decomposed in supercritical toluene at 450 °C. $Sn(HMDS)_2$ creates Sn nanoparticles that seed Si nanowire growth by the supercritical fluid–liquid–solid (SFLS) mechanism. The Si : Sn ratio in the reaction determines the growth of amorphous Si shell. No amorphous shell forms at relatively low Si : Sn ratios of 20 : 1, whereas higher Si : Sn ratio of 40 : 1 leads to significant amorphous shell. We propose that hydrogen evolved from trisilane decomposition etches away the Sn seed particles as nanowires grow, which promotes the amorphous Si shell deposition when the higher Si : Sn ratios are used.

Introduction

Silicon (Si) nanowires have properties suitable for a wide range of applications including photovoltaics,[1–3] field-effect transistors,[4,5] thermoelectric devices,[6,7] and lithium-ion batteries.[8–10] Solvent-based chemical synthetic routes—solution–liquid–solid (SLS)[11] and supercritical fluid–liquid–solid (SFLS)[12,13] methods—have been developed to produce the significant quantities of Si nanowires needed for many of these applications. These approaches use a solvent reaction medium, a reactant for the semiconductor, and metal nanoparticles as seeds to induce nanowire formation by a crystallization mechanism similar to vapor–liquid–solid (VLS) growth in the gas phase.[14] In SFLS synthesis, a colloidal suspension of metal seed particles is introduced with Si precursor into a hot, pressurized supercritical solvent, and so SFLS provides a higher temperature window than SLS since the reaction medium can be heated well above its ambient boiling temperature under pressure. SFLS growth is typically carried out as a semi-continuous process with nanowires forming in the bulk volume of the reactor, enabling significant quantities of nanowires to be produced. For example, a relatively small reactor volume of 10 mL can yield hundreds of milligrams of nanowires in minutes.[13] Gold (Au) has been the most effective and prominent seed metal for SFLS growth of Si nanowires because it has good chemical stability, a relatively low eutectic temperature with Si of 363 °C, and is easy to make in nanocrystal form.[15] However, Au is expensive and forms deep electronic traps in Si,[16] which is detrimental to the performance of electronic and optical Si devices.[17–19] As a result, there has been an emphasis on developing alternative metal seeds for Si nanowires.[15,20–23]

Tin (Sn) is an interesting alternative to Au, forming a lower temperature eutectic with Si at 232 °C with better electronic compatibility—Sn-related levels lie close to the Si band edge and Sn impurities are relatively benign in Si.[16] Sn has been used to seed Si nanowires by CVD-VLS growth.[3,24–28] For solution-based Si nanowire growth, colloidal Sn nanoparticles typically require relatively high molecular weight polymeric capping ligands,[29] which is not ideal for nanowire synthesis. Recently, we demonstrated SFLS growth of crystalline Si nanowires from trisilane (Si_3H_8) seeded by the addition of the Sn reactant, bis(bis(trimethylsilyl)amino)tin ($Sn(HMDS)_2$), instead of pre-synthesized Sn nanoparticles.[10] $Sn(HMDS)_2$ decomposes in the reactor to Sn seed nanoparticles that induce nanowire growth, which eliminates the preliminary nanocrystal synthesis step. This approach of *in situ* seed particle formation has also proven successful for growth of multiwall carbon nanotubes in supercritical fluids, using molecular precursors of ferrocene and cobaltocene for iron and cobalt.[30–32] In the multiwall carbon nanotube synthesis, the reaction conditions and reactant concentrations had a significant influence on nanotube quality and reaction product ranging from multiwall carbon nanotubes with highly graphitic shells to solid carbon fibers.[32] Here, we show that the Si nanowire synthesis conditions can be adjusted to yield either crystalline Si nanowires or Si nanowires composed of a crystalline core coated with an amorphous Si shell.

Amorphous Si coatings on crystalline Si nanowires have been shown to provide a variety of advantageous properties to the nanowires, including reduced surface recombination, increased light absorption, and enhanced mechanical properties, which are important for improving performance in

Department of Chemical Engineering, Texas Materials Institute, Center for Nano- and Molecular Science and Technology, The University of Texas at Austin, Austin, Texas 78712-1062, USA. E-mail: korgel@che.utexas.edu; Fax: +1-512-471-7060; Tel: +1-512-471-5633

applications including photovoltaics, transistors, and lithium-ion batteries.[33–38] Existing synthetic methods for Si nanowires with a crystalline core and amorphous shell produce nanowires tethered to a substrate with low yield and typically use Au seeds, thus limiting their use in practical applications.[25,33,35,36] The synthesis reported here provides a method for obtaining significant quantities of crystalline-amorphous core–shell Si nanowires that does not use Au as a seed.

Experimental details

Materials

All reagents and solvents were used as received without further purification. Dodecanethiol (DDT, ≥98%), tetrachloroaurate trihydrate (≥99.9%), sodium borohydride (≥98%), toluene (anhydrous, 99.8%), ethanol (EtOH, 99.9%), tetraoctylammonium bromide (TOAB, 98%), chloroform, and bis(bis(trimethylsilyl)amino)tin ($Sn(HMDS)_2$, lot 10396PKV) (99.8%) were purchased from Sigma-Aldrich. Trisilane (Si_3H_8, 100%) was purchased from Voltaix. (*Caution: Trisilane is pyrophoric and must be stored and handled under an inert atmosphere!*) Dodecanethiol-capped Au nanocrystals (2 nm diameter) were synthesized following the methods of Brust *et al.*[39] and stored in a nitrogen-filled gloved box dispersed in toluene at a concentration of 50 mg mL^{-1} prior to use.

Silicon nanowire synthesis

Si nanowires were prepared using either Au nanocrystal seeds or with Sn seeds generated *in situ* in the reactor from

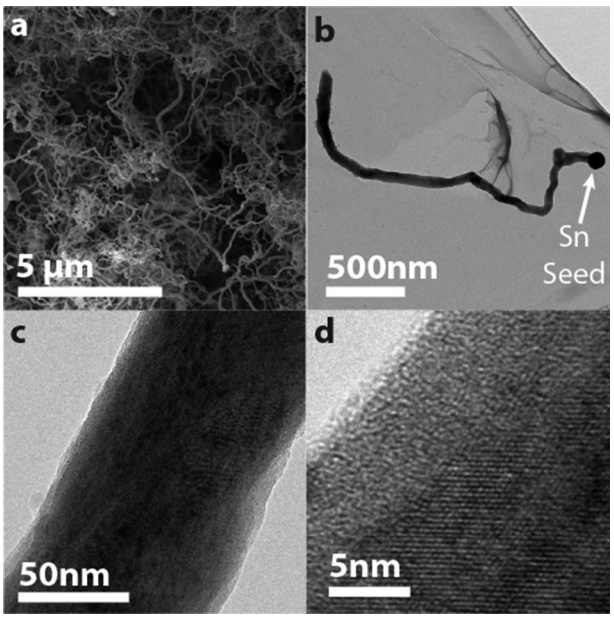

Fig. 1 (a) SEM and (b,c) TEM images of Sn-seeded Si nanowires. Most nanowires have Sn seed particles at their tips. The HRTEM image in (d) shows the crystalline core of a nanowire.

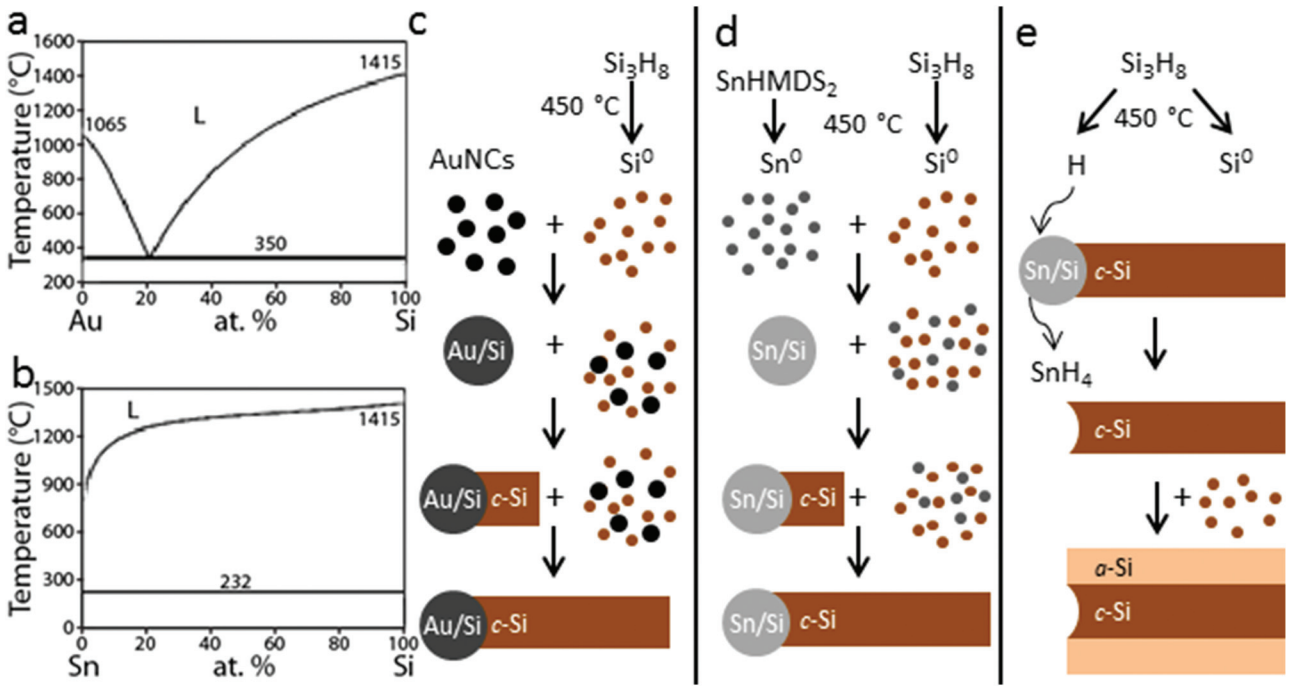

Fig. 2 Phase diagrams for (a) Au and Si and (b) Sn and Si. The reaction temperature of 450 °C exceeds both the Au : Si and Sn : Si eutectic temperatures. (c) The formation of Si nanowires from Au seed particles and trisilane. (d) The synthesis of Si nanowires from trisilane *via in situ* seeding with Sn. (e) With relatively high Si : Sn ratio, H evolved from trisilane decomposition reacts with Sn seed particles to form volatile tin hydrides (*e.g.* SnH_4 or Sn_2H_6), etching away the Sn seed particles during nanowire growth. Under these conditions, Si also deposits heterogeneously on the surface of the nanowires as an amorphous shell.

$Sn(HMDS)_2$. Au-seeded Si nanowires were synthesized in supercritical toluene using a flow-through high pressure sealed titanium reactor within a nitrogen-filled glovebox.[13] The reactor was preheated to 450 °C and pressurized with toluene to 6.9 MPa. For Si nanowires a reactant solution of 0.250 mL of trisilane, 0.550 mL of a 50 mg mL^{-1} Au nanocrystal dispersion in toluene, and an additional 0.300 mL of toluene was prepared in a 1 mL injection syringe. Crystalline Si nanowires without an amorphous shell were prepared using a reactant solution of 0.250 mL trisilane, 0.116 mL $Sn(HMDS)_2$, and 0.700 mL toluene. Si nanowires with amorphous Si shells were prepared with reactant solutions of 0.250 mL trisilane, 0.058 mL $Sn(HMDS)_2$, and 0.800 mL toluene. In each case, the reactant solution was injected at a rate of 3.0 mL min^{-1} for 1 min with a closed outlet, causing the reactor pressure to increase to 15.2 MPa. Immediately after injection, the inlet line is closed and the reactor is removed from the heating block and allowed to cool to room temperature. The reactor is removed from the glovebox and opened to extract the nanowires with additional toluene (~15 mL). The crude reaction product was precipitated by centrifugation at 8000 rpm for 5 min and the supernatant discarded and washed three times by repeated dispersion in a 2 : 1 : 1 chloroform–toluene–ethanol mixture, centrifugation, and decanting of the supernatant. After purification, the nanowires were dispersed in chloroform and stored under ambient conditions. A typical reaction yields 100 mg for Au-seeded Si nanowires and 80 mg of nanowires for both Sn-seeded synthesis methods.

Material characterization

Scanning electron microscopy (SEM) images were acquired using a Zeiss Supra 40 SEM with an in-lens arrangement, a working voltage of 2 kV and 5 mm working distance. SEM samples were prepared by drop-casting from chloroform dispersions onto a polished silicon wafer. Transmission electron microscopy (TEM) images were digitally acquired using a field emission JEOL 2010F TEM operated at 200 kV. TEM samples were prepared by drop-casting from chloroform dispersions onto 200 mesh lacey-carbon copper TEM grids (Electron Microscopy Sciences). Energy-dispersive X-ray spectroscopy (EDS) line scans were performed with an Oxford Inca EDS detector on the JEOL 2010F TEM operating in dark field scanning transmission electron microscopy (STEM) mode. X-ray diffraction (XRD) was performed with a Rigaku R-Axis Spider Diffractometer with Image plate detector and Cu-Kα (λ = 1.5418 Å) radiation operated at 40 kV and 40 mA. Samples were measured on a 0.5 mm nylon loop, scanning for 15 min with 1° per second sample rotation under ambient conditions. Diffraction data were radially integrated and background scattering from the nylon loop was subtracted.

Results and discussion

Fig. 1 shows high-resolution scanning electron microscopy (HRSEM) and high resolution transmission electron microscopy (HRTEM) images of Si nanowires synthesized by the addition of trisilane and $Sn(HMDS)_2$ into the reactor with a Si : Sn ratio of 20 : 1. $Sn(HMDS)_2$ decomposes in the reactor to form Sn nanoparticles that induce SFLS nanowire growth as illustrated in Fig. 2. The nanowires have diameters ranging from 80–120 nm and lengths of 1–10 μm. As shown in Fig. 1 and 3, TEM and XRD confirm that the nanowires are crystalline. The nanowires also have a significant amount of kinking and related twin defects. XRD peaks corresponding to Sn are also observed from nanowires made with relatively low Si : Sn ratios (~20 : 1) that did not have amorphous Si shells (Fig. 3b).

Increasing the Si : Sn ratio fed into the reactor to 40 : 1 results in the formation of crystalline Si nanowires with an amorphous Si shell (Fig. 4). SEM images (Fig. 4a) show nanowires with similar dimensions and morphology as those synthesized at lower Si : Sn ratios, but TEM images show that the nanowires have an amorphous Si shell about 30–50 nm thick coating a crystalline core ranging from 30 to 70 nm in diameter. Fig. 4c shows a typical TEM image of the interface between the amorphous shell and the crystalline core of a nanowire.

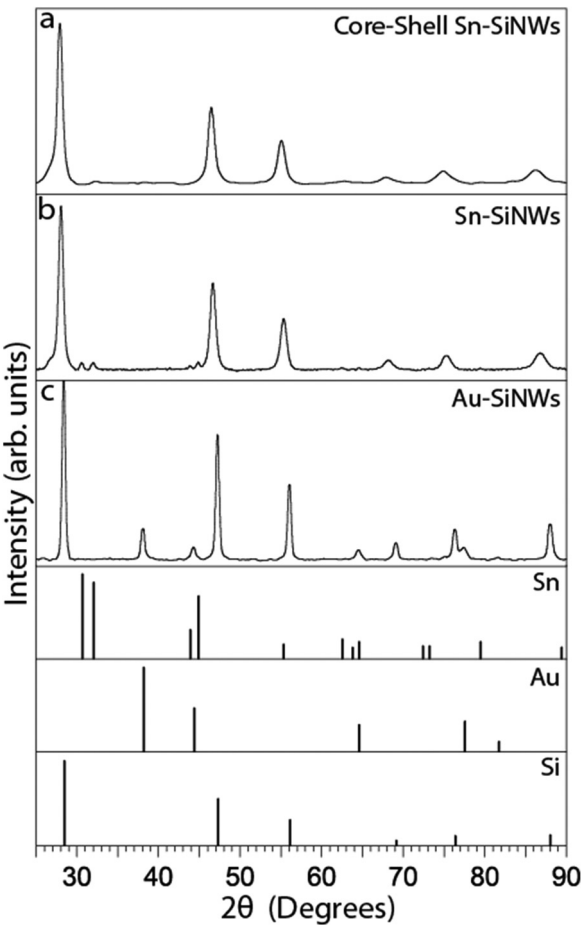

Fig. 3 XRD patterns for (a) Sn-seeded crystalline-amorphous core–shell Si nanowires, (b) Sn-seeded Si nanowires, and (c) Au-seeded Si nanowires with reference patterns for Sn, Au, and Si. (JCPDS: tetragonal β-Sn 00-004-0673, Au 00-004-0784, Si 00-027-1402).

Composition profiles of Si nanowires seeded with Au nanocrystals and Sn were obtained using dark field scanning transmission electron microscopy (STEM) coupled with energy-dispersive X-ray spectroscopy (EDS) and compared (Fig. 5).

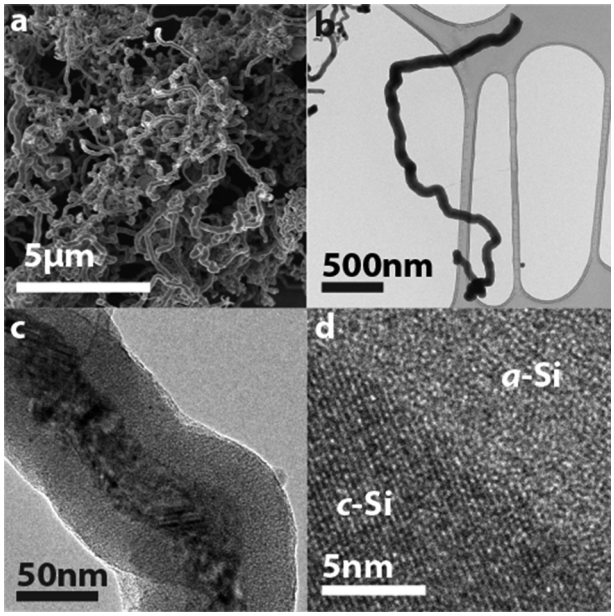

Fig. 4 (a) SEM and (b,c) TEM images of Sn-seeded crystalline-amorphous core–shell Si nanowires. The nanowires are highly kinked without Sn seed particles remaining at their tips after synthesis. (d) A HRTEM image showing the lattice fringes of the crystalline core and the amorphous shell.

TEM and SEM data of the Au-seeded Si nanowires are shown in Fig. 6. The EDS line scans confirmed that both the crystalline core and amorphous shell of nanowires made with Sn seeds are composed of Si. EDS line scans also revealed significant Sn in the crystalline core of the nanowires, whereas as there is no detectable Au in the Au-seeded nanowires. XRD of the core–shell nanowires seeded with Sn showed no Sn diffraction peaks (Fig. 3b), unlike the Si nanowires without an amorphous shell made at lower Si : Sn ratio. TEM also showed that the nanowires with amorphous Si shells did not have Sn seeds at their ends, suggesting that Sn seed particles are consumed during the reaction. At the higher Si : Sn ratio and without Sn at the end of the nanowires, trisilane decomposition led to heterogeneous deposition of a relatively thick amorphous Si on the surface of the nanowires.[40]

The EDS line scans showed that there is nearly 10 at% Sn in the crystalline nanowires and 3 at% Sn in the crystalline core of the core–shell nanowires. This is well above the solid solubility limit of Sn in Si at the growth temperature of 450 °C, which is 0.015 at% Sn.[41] The (111) XRD peaks observed for the Si nanowires seeded by Sn are also shifted to slightly lower diffraction angle than expected for diamond cubic Si, consistent with an expanded lattice due to the incorporation of Sn. 10 at% Sn in Si would be expected to shift the (111) peak from 2Θ = 28.44° to 27.88°, which is close to what is observed experimentally in Fig. 3.[42] The Au-seeded Si nanowires made with a similar Si : Au ratio of 40 : 1 (Fig. 6) had no Au in the core of the nanowire detectable by EDS and the XRD patterns index well to diamond cubic Si. The solid solubility of Au in Si

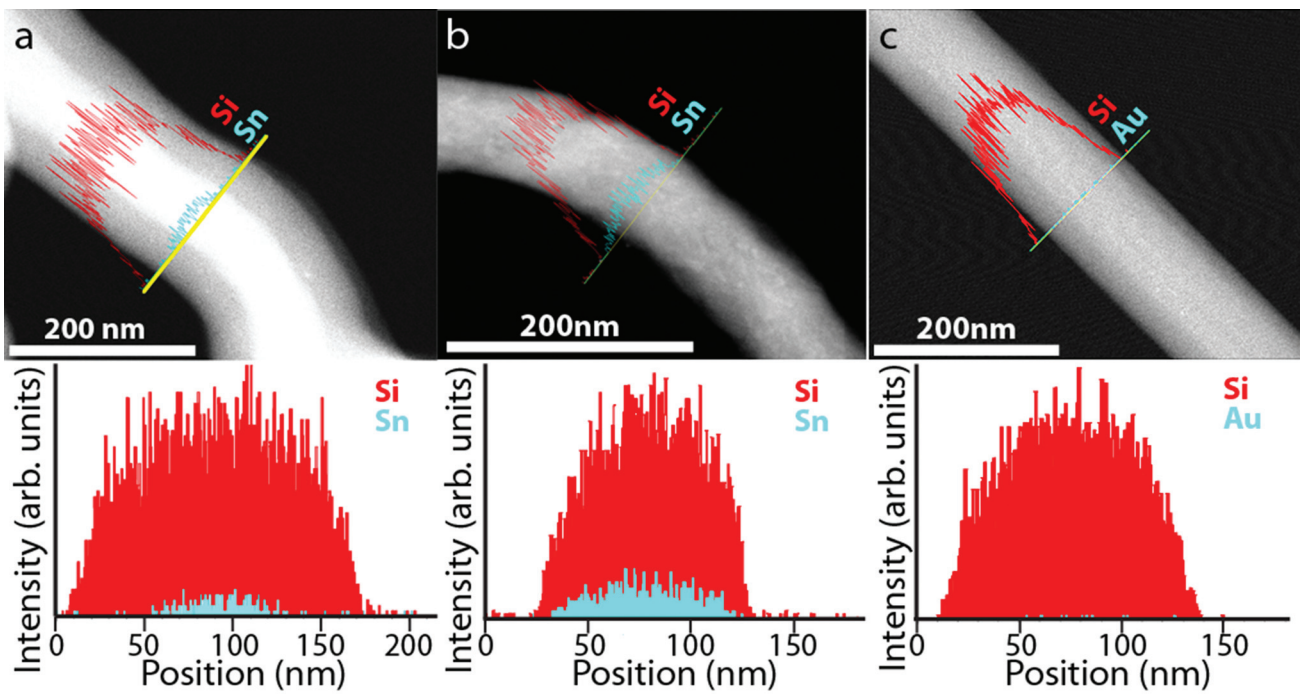

Fig. 5 Dark field STEM images of (a) Sn-seeded crystalline-amorphous core–shell Si nanowires, (b) Sn-seeded Si nanowires, and (c) Au-seeded Si nanowires. EDS line scan shows the presence of Sn in the crystalline core, but not in the amorphous shell of the Si nanowires. No Au was detected in the line scan across the Au-seeded Si nanowire.

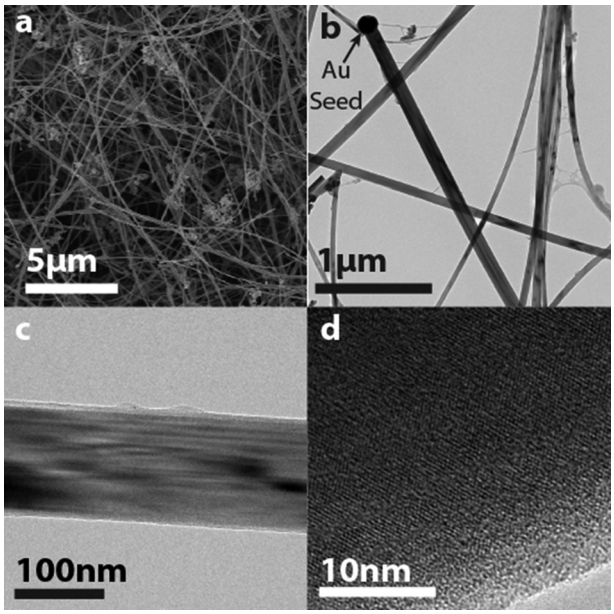

Fig. 6 (a) SEM and (b,c) TEM images of Au-seeded Si nanowires. The nanowires are long and straight, unlike Sn seeded wires, and have a large Au seed particle remaining after synthesis. (d) HRTEM image shows lattice fringes of the highly crystalline nanowires.

at 450 °C is also very low—less than 0.01 ppm.[43] Recent studies have shown that metal atoms from seeding particles can incorporate at grain boundaries and crystal defects in nanowires.[44,45] The reason for the significant amount of Sn incorporation in the Si nanowires here is not clear and requires further study, but certainly would also contribute to the loss of Sn at the tips of the nanowires during growth. No Sn was observed in the amorphous shell of the nanowires.

The absence of the Sn seed is also consistent with etching by hydrogen during nanowire growth. Rathi *et al.*[24] found that in their plasma enhanced CVD VLS growth of Si nanowires with Sn seeds, the H_2 plasma reacted with Sn to form volatile tin hydrides (*e.g.* SnH_4 or Sn_2H_6) and the loss of Sn would ultimately arrest wire growth. Similarly, it is likely that hydrogen evolved from trisilane decomposition reacts with the Sn during the SFLS growth process. While there is sufficient Sn in the reactor to continually seed nanowire growth at the lower Si : Sn ratio despite some dissolution to the hydrogen, at higher Si : Sn ratios, hydrogen appears to completely dissolve away the Sn seeds, thereby contributing to the formation of the amorphous Si shell.

Conclusions

$Sn(HMDS)_2$ was used for *in situ* Sn seeding of Si nanowires from trisilane in supercritical toluene *via* the SFLS growth mechanism. TEM showed the presence of Sn particles on the tips of wires confirming the decomposition of $Sn(HMDS)_2$ into Sn seed particles. Excess hydrogen produced from trisilane decomposition at high Si : Sn ratios was found to dissolve away the Sn seed particle during synthesis, leading in part to the formation of crystalline-amorphous core–shell Si nanowires. Dark field STEM imaging and EDS line scans found the inclusion of significant amounts of Sn in the crystalline portion of the Si nanowires, unlike the case of the Au-seeded nanowires. The Sn concentration in the crystalline Si nanowires was found to significantly exceed the solid solubility at the growth temperature.

Acknowledgements

This work was funded by the Robert A. Welch Foundation (grant no. F-1464) and as part of the program "Understanding Charge Separation and Transfer at Interfaces in Energy Materials (EFRC: CST)", an Energy Frontier Research Center funded by the U.S. Department of Energy Office of Science, Office of Basic Energy Sciences, under Award No. DE-SC0001091. T.D.B acknowledges the National Defense Science and Engineering Graduate Fellowship for financial support. The authors thank J.P. Zhou for HRTEM assistance and Aaron Chockla for helpful discussions about the Sn-seeded Si nanowire reaction.

Notes and references

1 T. Stelzner, M. Pietsch, G. Andrä, F. Falk, E. Ose and S. Christiansen, *Nanotechnology*, 2008, **19**, 295203.
2 V. Sivakov, G. Andrä, A. Gawlik, A. Berger, J. Plentz, F. Falk and S. H. Christiansen, *Nano Lett.*, 2009, **9**, 1549–1554.
3 M. Jeon and K. Kamisako, *Mater. Lett.*, 2009, **63**, 777–779.
4 W. S. Wong, S. Raychaudhuri, R. Lujan, S. Sambandan and R. A. Street, *Nano Lett.*, 2011, **11**, 2214–2218.
5 Y. Paska, T. Stelzner, O. Assad, U. Tisch, S. Christiansen and H. Haick, *ACS Nano*, 2012, **6**, 335–345.
6 A. I. Hochbaum, R. Chen, R. D. Delgado, W. Liang, E. C. Garnett, M. Najarian, A. Majumdar and P. Yang, *Nature*, 2008, **451**, 163–167.
7 L. D. Hicks and M. S. Dresselhaus, *Phys. Rev. B: Condens. Matter*, 1993, **47**, 16631–16634.
8 A. M. Chockla, T. D. Bogart, C. M. Hessel, K. C. Klavetter, C. B. Mullins and B. A. Korgel, *J. Phys. Chem. C*, 2012, **116**, 18079–18086.
9 A. M. Chockla, J. T. Harris, V. A. Akhavan, T. D. Bogart, V. C. Holmberg, C. Steinhagen, C. B. Mullins, K. J. Stevenson and B. A. Korgel, *J. Am. Chem. Soc.*, 2011, **133**, 20914–20921.
10 A. M. Chockla, K. C. Klavetter, C. B. Mullins and B. A. Korgel, *Chem. Mater.*, 2012, **24**, 3738–3745.
11 A. T. Heitsch, D. D. Fanfair, H.-Y. Tuan and B. A. Korgel, *J. Am. Chem. Soc.*, 2008, **130**, 5436–5437.
12 J. D. Holmes, K. P. Johnston, R. C. Doty and B. A. Korgel, *Science*, 2000, **287**, 1471–1473.
13 A. T. Heitsch, V. A. Akhavan and B. A. Korgel, *Chem. Mater.*, 2011, **23**, 2697–2699.

14 B. A. Korgel, *AIChE J.*, 2009, **42**, 842–848.
15 V. Schmidt, J. V. Wittemann and U. Gösele, *Chem. Rev.*, 2010, **110**, 361–388.
16 S. M. Sze and K. K. Ng, *Physics of Semiconductor Devices*, Wiley, New York, 2nd edn, 1981.
17 J. E. Allen, E. R. Hemesath, D. E. Perea, J. L. Lensch-Falk, Z. Y. Li, F. Yin, M. H. Gass, P. Wang, A. L. Bleloch, R. E. Palmer and L. J. Lauhon, *Nat. Nanotechnol*, 2008, **3**, 168–173.
18 K. Watanabe and C. Munakata, *Semicond. Sci. Technol.*, 1993, **8**, 230.
19 W. M. Bullis, *Solid-State Electron.*, 1966, **9**, 143–168.
20 F.-W. Yuan, H.-J. Yang and H.-Y. Tuan, *J. Mater. Chem.*, 2011, **21**, 13793–13800.
21 H.-Y. Tuan, D. C. Lee, T. Hanrath and B. A. Korgel, *Nano Lett.*, 2005, **5**, 681–684.
22 H.-Y. Tuan, D. C. Lee and B. A. Korgel, *Angew. Chem., Int. Ed.*, 2006, **45**, 5184–5187.
23 H.-Y. Tuan, A. Ghezelbash and B. A. Korgel, *Chem. Mater.*, 2008, **20**, 2306–2313.
24 S. J. Rathi, B. N. Jariwala, J. D. Beach, P. Stradins, P. C. Taylor, X. Weng, Y. Ke, J. M. Redwing, S. Agarwal and R. T. Collins, *J. Phys. Chem. C*, 2011, **115**, 3833–3839.
25 S. Cheng, T. Ren, P. Ying, R. Yu, W. Zhang, J. Zhang and C. Li, *Sci. China Chem.*, 2012, **55**, 2573–2579.
26 L. Yu, B. O'Donnell, P.-J. Alet, S. Conesa-Boj, F. Peiró, J. Arbiol and P. R. I. Cabarrocas, *Nanotechnology*, 2009, **20**, 225604.
27 E. Mullane, T. Kennedy, H. Geaney, C. Dickinson and K. M. Ryan, *Chem. Mater.*, 2013, DOI: 10.1021/cm400367v, Article ASAP.
28 H. Geaney, E. Mullane, Q. M. Ramasse and K. M. Ryan, *Nano Lett.*, 2013, **13**, 1675–1680.
29 N. H. Chou and R. E. Schaak, *J. Am. Chem. Soc.*, 2007, **129**, 7339–7345.
30 D. C. Lee, F. V. Mikulec and B. A. Korgel, *J. Am. Chem. Soc.*, 2004, **126**, 4951–4957.
31 D. K. Smith, D. C. Lee and B. A. Korgel, *Chem. Mater.*, 2006, **18**, 3356–3364.
32 D. C. Lee and B. A. Korgel, *Mol. Simul.*, 2005, **31**, 637–642.
33 H. Chen, J. Xu, P. Chen, X. Fang, J. Qiu, Y. Fu and C. Zhou, *ACS Nano*, 2011, **5**, 8383–8390.
34 M. M. Adachi, M. P. Anantram and K. S. Karim, *Nano Lett.*, 2010, **10**, 4093–4098.
35 L.-F. Cui, R. Ruffo, C. K. Chan, H. Peng and Y. Cui, *Nano Lett.*, 2009, **9**, 491–495.
36 S. Khachadorian, K. Papagelis, K. Ogata, S. Hofmann, M. R. Phillips and C. Thomsen, *J. Phys. Chem. C*, 2013, **117**, 4219–4226.
37 Y. Dan, K. Seo, K. Takei, J. H. Meza, A. Javey and K. B. Crozier, *Nano Lett.*, 2011, **11**, 2527–2532.
38 Y. Dong, G. Yu, M. C. McAlpine, W. Lu and C. M. Lieber, *Nano Lett.*, 2008, **8**, 386–391.
39 M. Brust, M. Walker, D. Bethell, D. J. Schiffrin and R. Whyman, *J. Chem. Soc., Chem. Commun.*, 1994, 801–802.
40 J. T. Harris, J. L. Hueso and B. A. Korgel, *Chem. Mater.*, 2010, **22**, 6378–6383.
41 R. W. Olesinski and G. J. Abbaschian, *Bull. Alloy Phase Diagrams*, 1984, **5**, 273–276.
42 The (111) peak for diamond cubic Sn is expected at 2Θ = 23.70°.
43 H. Okamoto and T. B. Massalski, *Bull. Alloy Phase Diagrams*, 1983, **4**, 190–198.
44 J. E. Allen, E. R. Hemesath, D. E. Perea, J. L. Lensch-Falk, Z. Y. Li, F. Yin, M. H. Gass, P. Wang, A. L. Bleloch, R. E. Palmer and L. J. Lauhon, *Nat. Nanotechnol.*, 2008, **3**, 168–173.
45 E. R. Hemesath, D. K. Schreiber, E. B. Gulsoy, C. F. Kisielowski, A. K. Petford-Long, P. W. Voorhees and L. J. Lauhon, *Nano Lett.*, 2012, **12**, 167–171.